RSC Advances

PAPER

View Article Online
View Journal | View Issue

Cite this: *RSC Adv.*, 2015, **5**, 58514

Carbon nanotube-assisted growth of single-/multi-layer SnS_2 and SnO_2 nanoflakes for high-performance lithium storage†

Dongsheng Guan, Jianyang Li, Xianfeng Gao and Chris Yuan*

SnS_2 nanoparticles and SnS_2 nanoflake/CNTs composite are prepared by a low-cost facile hydrothermal method for their use in rechargeable Li-ion batteries. It is found that the presence of multi-walled CNTs during synthesis greatly affects the morphology of as-formed SnS_2 nanostructures, and circinal single-layer and multilayer SnS_2 nanoflakes enwrapped by CNTs are produced. The composite is further oxidized to porous SnO_2 nanoflake/CNTs hybrid by annealing at 500 °C in air. The formation mechanism of SnS_2/CNTs and SnO_2/CNTs composites is examined. All the three materials are used as the anode in Li-ion batteries. The SnS_2/CNTs composite delivers stronger cycling stability than the pure SnS_2 anode. In tests the former exhibits excellent capacity retention of 91.5% at 100 mA g^{-1} over 50 cycles, while the latter displays 66.8%. The rate capability of SnS_2/CNTs composite is much better than pure SnS_2 as well. Redox reaction characteristics and Li-ion transfer kinetics at the two SnS_2 anodes are studied by differential capacity plots and electrochemical impedance spectroscopy. It is discovered that the SnS_2/CNTs composite with larger surface area allows faster Li-ion transfer kinetics, effective cushion of volume changes, and thus gains the improved Li-ion intercalation behaviours. The capacity of the tin-based anode can be further raised by transformation to a SnO_2/CNTs hybrid that also delivers excellent rate and cycling performances.

Received 23rd May 2015
Accepted 26th June 2015

DOI: 10.1039/c5ra09613h

www.rsc.org/advances

1. Introduction

Currently, the soaring development of electronic devices and electric vehicles urgently demands novel mobile power sources with high energy and power density, good safety and durability. Rechargeable Li-ion batteries (LIBs) have become a candidate due to their large energy storage density, light weight, low self-discharge and long cycle life, no memory effects.[1,2] Graphite is the most commonly-used anode material in current commercial LIBs, but the low capacity and poor safety of graphite fail to meet the demand of next-generation LIBs, so a group of novel anode materials have been developed to replace it, including metal sulphides and oxides.[3–6] Among them, tin and tin-based materials such as tin alloys, tin oxides and tin sulphides are considered as potential anode materials for LIBs mostly owing to their large theoretical capacity and good reversibility. Tin disulphide (SnS_2) is an extensively-studied anode material with a layered hexagonal CdI_2-type structure, in which sheets of tin atoms are sandwiched between two close packed sheets of sulphur atoms, and they are bound by weak van der Waals forces.[7] A group of SnS_2 nanostructures, such as nanoparticles,[8] nanoplates,[9] nanosheets,[10] nanobelts,[11] nanoflower and nanorods,[12,13] have been synthesized by methods including hydrothermal and solvothermal methods, thermal sulfurization, wet chemistry and vapor deposition. In the practice it is found that SnS_2 with a theoretical capacity of 645 mA h g^{-1} suffers a large volume change (≥200%) and particle aggregation related to Li-ion insertion/extraction process, which leads to electrode pulverization and a loss of effective contact between the active material and in turn results in drastic capacity decay and poor cyclability.[14] In addition, low conductivity of SnS_2 (10^{-12}–10^{-2} S cm^{-1}) highly impedes electronic transfer and deteriorates its rate performance. A number of approaches are proposed to alleviate these problems. Among them, carbonaceous materials are often used to enhance the electrochemical performance of SnS_2. Kim *et al.* achieved carbon-coated SnS_2 nanoparticles that show far better Li-ion intercalation behaviour than uncoated SnS_2.[15] He *et al.* synthesized acetylene black incorporated SnS_2 nanoflower with increased Li-ion storage capacities.[16] Zhai *et al.* produced SnS_2 nanosheet anchored MWCNTs and found that the hybrid delivers higher capacity and cyclability than both the MWCNTs and SnS_2.[17] Sun *et al.* also fabricated SnS_2 nanoflake decorated MWCNTs with improved capacity and cycling performance.[18] Kang *et al.* discovered self-supported SnS_2 nanosheet coated MWCNTs with higher capacity and capability than pure SnS_2 nanosheets.[19] Tin dioxide (SnO_2) is an attractive

Department of Mechanical Engineering, University of Wisconsin Milwaukee, Milwaukee, USA 53211. E-mail: cyuan@uwm.edu; Fax: +1 414 229 5639; Tel: +1 414 229 6958

† Electronic supplementary information (ESI) available: SEM photos, BET curves, EDS spectrum, XPS spectra. See DOI: 10.1039/c5ra09613h

anode material as well, due to its high theoretical capacity of 781 mA h g^{-1}, but its huge volume change during Li-ion storage process results in a big loss of reversible capacity. Therefore, various methods are invented to solve this problem, such as SnO_2 coatings on TiO_2–B nanowires,[20] CNTs and graphene.[21,22] Those carbon materials not only give birth to new SnS_2 or SnO_2 nanostructures but also favor charge transfer and electrode stability, yielding improved Li-ion battery performances. So far, a new type of composites consisting of two-dimensional (2D) electrode materials and CNTs network has been reported, including MoS_2 nanosheet/MWCNTs,[3] CoOOH nanoplate/MWCNTs and $Ni(OH)_2$ nanoplate/MWCNTs.[23,24] The nanosheets or nanoplates embed into the porous matrix and connect conducting MWCNTs to achieve enhanced redox reaction kinetics and electronic conductivity, and finally obtain improved electrochemical properties. To the best of our knowledge, the composite composed of 2D SnS_2 or SnO_2 nanoflakes dispersed in such a CNTs network for LIBs applications has not been reported hitherto. We consider that CNTs can not only improve the conductivity of SnS_2 or SnO_2, but cushion the volume change and retard the agglomeration of the active material, which is possible to achieve novel tin-based anodes with high capacity, good cyclability and rate capability.

In the present work, we synthesized SnS_2 nanoparticles, SnS_2 nanoflake/CNTs and SnO_2 nanoflake/CNTs hybrids by scalable hydrothermal method and annealing. MWCNTs were found to promote the 2D growth of single-/multi-layer SnS_2 nanoflakes, improve the ionic and electronic transfer of electrodes. The thin nanoflakes can minimize the volume change during cycling for better cyclability and provide more sites to accommodate Li-ion insertion for increased capacities. A post heat treatment of these SnS_2/CNTs composite in air yielded a new SnO_2/CNTs hybrid that inherited the porous, nanoflake-like features, and exhibited further increased specific capacities.

2. Results and discussion

Fig. 1 shows XRD patterns of as-prepared SnS_2, SnS_2/CNTs and SnO_2/CNTs composites. In the pattern of SnS_2 diffraction peaks (001), (100), (101), (102), (110), (111), (103), (200), (201), (202) and (113) of hexagonal SnS_2 (JCPDS no. 23-0677, space group $P\bar{3}m1$) are observed at the 2θ angles of 15.1°, 28.3°, 32.2°, 41.9°, 50.1°, 52.5°, 55°, 58.5°, 60.9°, 67.2° and 70.4°, which demonstrates good crystallization of SnS_2 during hydrothermal process. The XRD pattern of SnS_2/CNTs hybrid is almost the same as that of SnS_2, with no peaks corresponding to MWCNTs, but the SnO_2/CNTs composite gives a different pattern. Typical peaks at the 2θ angle of 26.6°, 33.9°, 38°, 51.9°, 54.7°, and 64.8° are indexed to (110), (101), (200), (211), (220) and (112) crystal planes of tetragonal SnO_2 (JCPDS no. 41-1445, space group $P42/mnm$). Again, no diffraction peaks that belong to MWCNTs are identified from the pattern of SnO_2/CNTs. It is noted that the characteristics of XRD patterns of SnS_2 and SnO_2 (an oxidation product of SnS_2) here are in agreement with phase change described in previous reports.[25,26]

Fig. 2 presents SEM images of SnS_2, SnS_2/CNTs and SnO_2/CNTs materials. It is clearly seen that the absence of

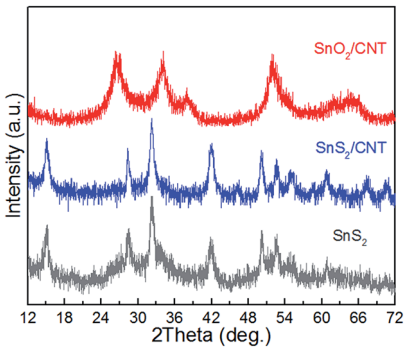

Fig. 1 X-ray diffraction patterns of SnS_2, SnS_2/CNTs and SnO_2/CNTs composites.

MWCNTs yields a big number of SnS_2 nanoparticles mostly with irregular shape and size (Fig. 2a). Some particles display an appearance of hexagonal nanoplates, indicating non-uniform growth of SnS_2 nanostructures under the hydrothermal conditions. An enlarged view of one SnS_2 nanoplate reveals its lateral size up to 650 nm and thickness up to ~100 nm (Fig. 2b). The presence of MWCNTs during synthesis leads to formation of a distinct nanostructure. As shown in Fig. 2c, considerable 2D SnS_2 nanoflakes are enwrapped by MWCNTs to form a porous SnS_2/CNTs hybrid structure. The nanoflakes are dense and thin, with a single layer or multiple layers. The multilayer nanoflake is constructed by small flakes developing around the centre of large flakes or underneath (Fig. 2d and S1a†). MWCNTs either insert into the flakes parallel or spread over them to bundle nanoflakes into their conductive network, rather than being coated or anchored with SnS_2.[17,18] The flakes display more uniform shapes, with a diameter up to 600 nm and a thickness of 10 nm (Fig. S1b†), which claims that SnS_2 prefers 2D growth mode along neighbouring CNTs when the two coexist in the superhot solution system. It is believed that the structure of 2D nanoflakes and loose CNTs network can possess larger specific surface than SnS_2 nanoparticles that are large and aggregated. In fact, BET measurements demonstrate that the surface area is 15.48 m^2 g^{-1} for pure SnS_2 and 47.87 m^2 g^{-1} for the SnS_2/CNTs (twice larger) (Fig. S2†). After annealing, SnS_2 is oxidized to be thin SnO_2 nanoflakes enwrapped in the CNT network (Fig. 2e). The nanoflake/CNTs structure is preserved, but the nanoflakes become porous and rough, which contain numerous tiny SnO_2 crystallites (Fig. 2f). Hence it is deduced that the oxide particles are supposed to originate from SnS_2 crystals and connect with each other to maintain the nanoflake-like shape. Excellent Li-intercalation behaviours of the two composites are expected, because the conductive MWCNTs, thin nanoflakes and porous structure are considered to endow fast charge transfer and small electrode resistance.[23,24]

The two nanoflake/CNTs composites are further observed by TEM. Fig. 3a shows a SnS_2 nanoflake conjunct CNTs. It has multiple layers, with several slim CNTs across its surface or underneath. An enlarged TEM image reveals that all the three-layer flakes are actually composed of nanoparticles (Fig. 3b). These particles are SnS_2 polycrystallites clearly seen in Fig. 3c. A

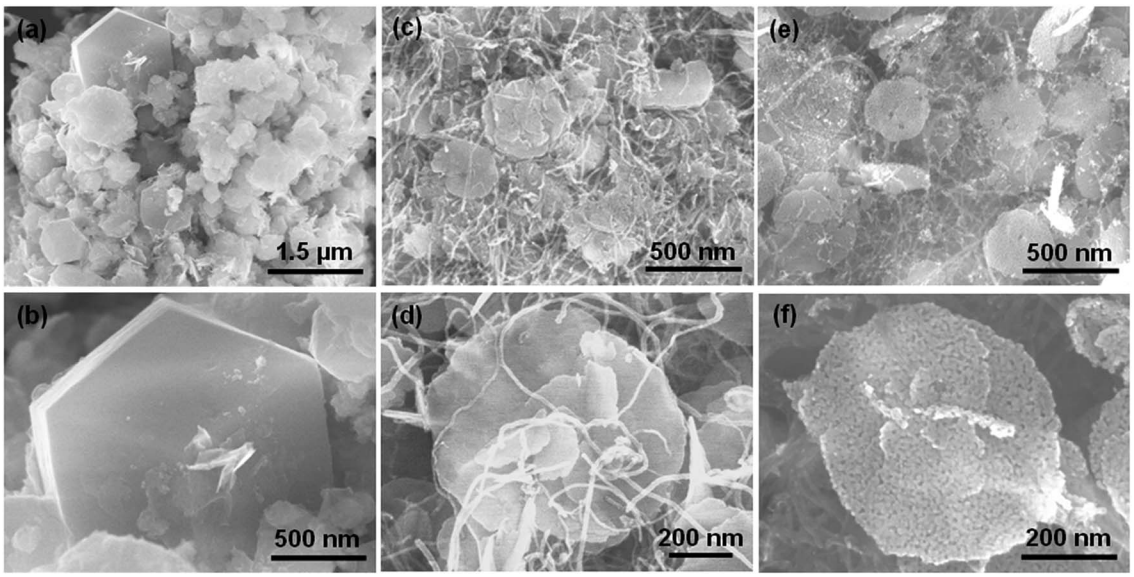

Fig. 2 SEM images of (a and b) pure SnS_2 particles, (c and d) SnS_2/CNTs composite and (e and f) SnO_2/CNTs composite.

selected area electron diffraction ring pattern of this part shows multiple indices (100), (101), (102), (110) and (201) of SnS_2 (Fig. 3d), which agrees well with the XRD index above.

Upon annealing SnS_2 is oxidized and a SnO_2/CNTs composite results. Both the nanoflake and CNTs survive (Fig. 4a). The enlarged view of spot C in Fig. 4a shows that the nanoflake is also composed of considerable nanoparticles (Fig. 4b), which is corresponding to our SEM observation above. They are SnO_2 polycrystallites with a size of ~5 nm (Fig. 4c). The selected area electron diffraction ring patterns reveals the (110), (101), (211) and (112) crystal planes of SnO_2 in this nanoflake (Fig. 4d).

EDS analyses were performed on the SnS_2/CNTs composite under SEM observation. In the spectrum in Fig. 5, distinct peaks between 3.3 and 4.1 keV correspond to the tin element. Sulfur peak appears at a position of 2.4 keV. Carbon is also found in this pattern, which is believed to be mostly from CNTs. A small peak belonging to oxygen is found, indicative of existence of

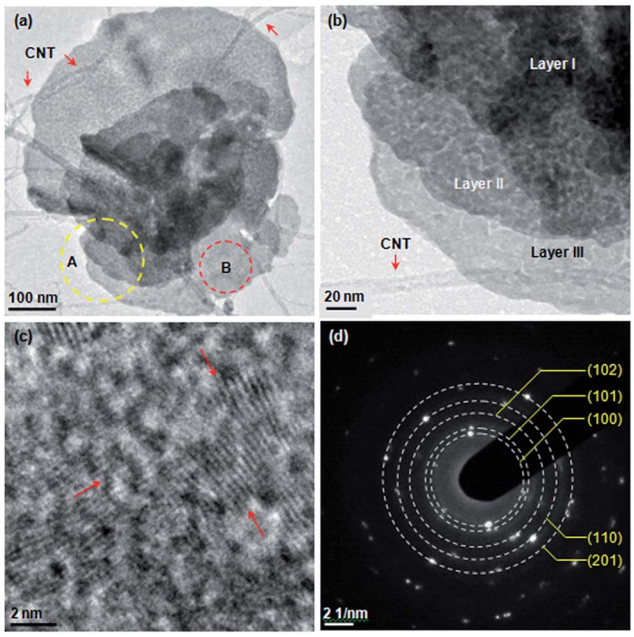

Fig. 3 TEM observation of SnS_2/CNTs composite: (a) SnS_2 nanoflake under low magnification, (b) SnS_2 nanoflake under high magnification of A spot in (a), (c) crystallites seen from B spot in (a), and (d) electron diffraction ring pattern taken from B spot with Miller indices of SnS_2.

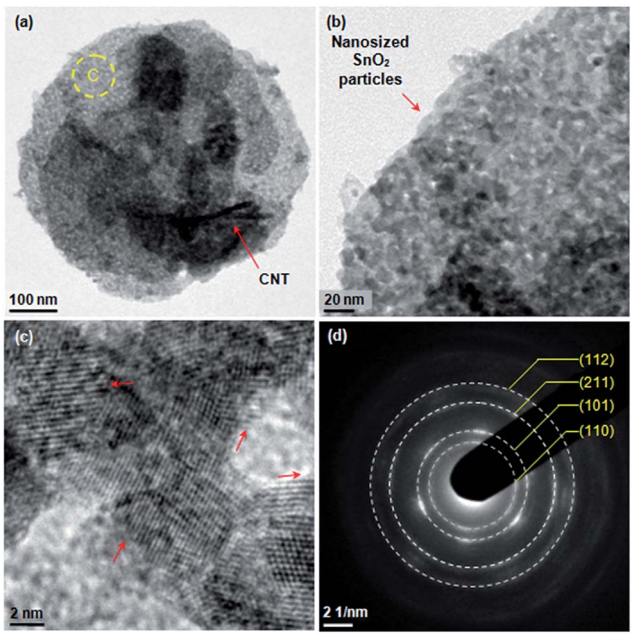

Fig. 4 TEM observation of SnO_2/CNTs composite: (a) SnO_2 nanoflake under low magnification, (b) SnO_2 nanoflake under high magnification of spot C in (a), (c) multiple crystallites in the nanoflake, and (d) electron diffraction rings taken from this spot with Miller indices of SnO_2.

oxygen species due to acid treatment. Al peak is from the holder used for placing the sample during observation. A linear scan of a multilayer nanoflake vividly tells that tin and sulphur are dominant elements there with a negligible amount of carbon and oxygen (Fig. 5b), which is corresponding to the aforementioned XRD pattern of the SnS_2/CNTs sample. After annealing in air, SnS_2 in the composite is completely oxidized to SnO_2, as evidenced by the disappearance of sulphur peak and the birth of stronger oxygen peak in the EDS spectrum of the SnO_2/CNTs composite (Fig. S3†).

The composition of two composites is further investigated by XPS technique. As for the SnS_2/CNTs sample, the peaks at 486.86, 495.26 and 161.7 eV in the high-resolution XPS spectra (Fig. 6a and b) are assigned to Sn 3d5/2, Sn 3d3/2 and S 2p, respectively. The energy difference between two tin peaks is 8.4 eV, indicating the existence of Sn(IV). The results confirm the SnS_2 compound in the composite. The broad C 1s peak at 284.8 eV is asymmetric (Fig. 6c), which is consisting of four subpeaks at 283.8, 284.3, 285.4 and 288.4 eV (Fig. S4a†). The peak at 283.8 and 284.3 eV could be assigned to sp^2 C=C bond and sp^3 C–C bond, either in a graphite phase or in an amorphous phase.[16] Peaks at 285.4 and 288.4 eV indicate the existence of residual groups such as –OH and –O–C=O, probably due to the acid treatment of CNTs and the adsorbed reactant.[16] Likewise, Sn(IV) is detected in the SnO_2/CNTs composite but sulphur not (Fig. 6d). It can be seen in Fig. 6b that broad O 1s peak at 531.3 eV is composed of three subpeaks at 530.5 eV (Sn–O bond), 531.6 eV (Sn–O–C bond) and 532.9 eV (C–O bond)[27] (Fig. S4b†). C 1s XPS peak from the SnO_2/CNTs is asymmetric as well at 284.6 eV (Fig. 6f), which includes three subpeaks at 283.8 eV (C=C bond), 284.6 eV (C–C bond), 285.3 eV (C–O bond) and 288.4 eV (O–C=O bond) as shown in Fig. S4c.† Thereby, it can be easily concluded that SnS_2 and SnO_2 nanoflakes have been successfully produced and incorporated into the CNTs network by hydrothermal means and annealing in oxidative atmosphere.

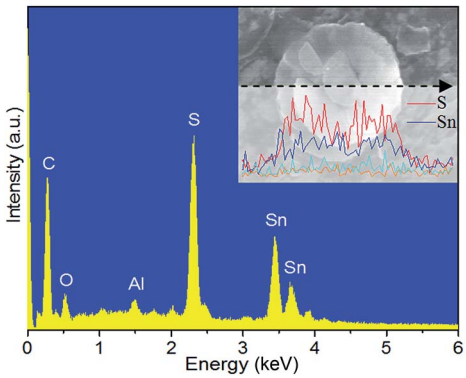

Fig. 5 EDS spectrum of SnS_2/CNTs composite. The inset is elemental linear scan across a single SnS_2 nanoflake.

The percentages of CNTs in the SnS_2/CNTs and SnO_2/CNTs composites were determined by TG analysis in air atmosphere, as shown in Fig. 7. The data presented in Fig. 7a reveals that the TG plot of SnS_2/CNTs hybrid shows a three-step mass-loss process. A small weight loss of ~1% from room temperature to 200 °C can be attributed to the removal of physically adsorbed water. The next weight loss step between 200 °C and 560 °C is ascribed to the oxidation of SnS_2 into SnO_2.[18] The third weight loss observed from 560 °C to 800 °C is owing to the burning of CNTs in the composite.[28] The total weight loss suffered by the composite is 35.4%. As for the SnO_2/CNTs hybrid, the drastic weight loss of 16% observed from 560 °C to 800 °C results from the burning of MWCNTs (Fig. 7b). This confirms that the second weight loss of SnS_2/CNTs hybrid is truly owing to the oxidation of SnS_2 to SnO_2. As a result, the weight fraction of CNTs in the SnS_2/CNTs and SnO_2/CNTs is estimated to be *ca.*

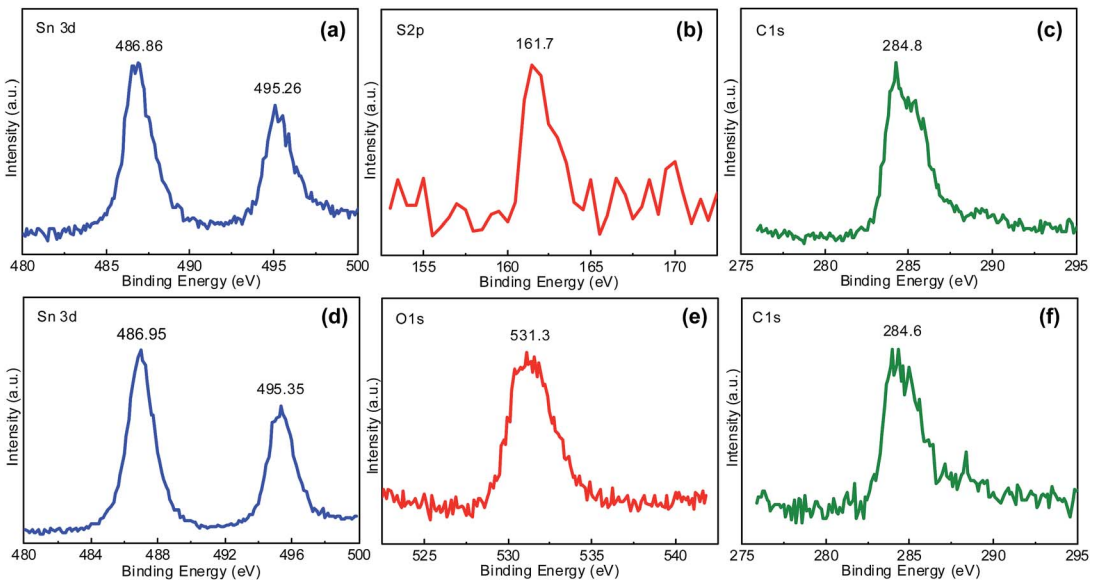

Fig. 6 XPS spectra of (a) Sn 3d, (b) S 2p, (c) C 1s signals taken from SnS_2/CNTs composite, of (d) Sn 3d, (e) O 1s and (f) C 1s signals taken from SnO_2/CNTs composite.

14% and 16%, respectively. The high ratio of CNTs is likely to contribute to the advantage of constructing conductive network for enhanced tin-based anode performance.

Based on above analyses, the probable growth process of the two composites is discussed with schematic illustration shown in Fig. 8. The formation of tin sulfide (SnS) precursors may be described as follows:[12]

$$Sn^{2+} + 2C_2H_5OH \rightarrow 2Sn(C_2H_5O)_2 + 2H^+ \quad (1)$$

$$NH_2CSNH_2 + 4C_2H_5OH \rightarrow 2NH_3\uparrow + 2C_2H_5OC_2H_5 + CO_2 + H_2S \quad (2)$$

$$H_2S + Sn(C_2H_5O)_2 \rightarrow SnS + 2C_2H_5OH \quad (3)$$

It is noted that eqn (2) takes place in the presence of H^+ in the superhot solution.[12] We know that increasing the temperature encourages the oxidation reaction of Sn^{2+} to Sn^{4+}; when the temperature goes up to 140 °C and more, SnS_2 originates from SnS.[29] Thus, we speculate that SnS forms initially and it is then oxidized to SnS_2 in the aid of excessive sulfur sources. Hence, the formation of many SnS_2 nuclei occurs in the hydrothermal process. They grow and start to agglomerate with each other. The further growth of these agglomerates is restricted fairly by dispersed CNTs, so they prefer to develop parallel to the CNTs, eventually yielding uniform thin nanoflakes inside the CNTs network (Fig. 8). Upon heat treatment in air, SnS_2 nanoflakes are oxidized *in situ* to form SnO_2 nanoflakes in the network.

In this study the Li-ion intercalation behaviour of SnS_2 and SnS_2/CNTs hybrids are first compared to investigate the effects of MWCNTs on the electrochemical property. The potential of redox reactions is studied *via* charge–discharge plots measured at 100 mA g^{-1} (Fig. 9a and b). Both electrodes have large initial discharge capacity; namely, 1161.2 mA h g^{-1} for SnS_2 anode and 1430.5 mA h g^{-1} for SnS_2/CNTs anode. Afterward, a rapid decline of discharge capacity occurs in the first two cycles for both electrodes, mostly due to the decomposition of electrolyte components and formation of solid-electrolyte-interface (SEI) layers on electrode surface, or the irreversible Li-ion insertion into the electrode materials (Li^+ rapping effects).[30] In the charge plots, a slowly increasing potential plateau is seen starting from 0.38 V to 0.7 V. It is well known that the lithiation/delithiation reactions in SnS_2 have two steps and can be described by:[16]

$$SnS_2 + 4Li^+ + 4e^- \rightarrow Sn + 2Li_2S \quad (4)$$

$$Sn + xLi^+ + xe^- \leftrightarrow Li_xSn\ (0 \le x \le 4.4) \quad (5)$$

In the first step, Li-ion insertion into SnS_2 forms metallic Sn and amorphous Li_2S. In following discharge–charge cycles, the alloy and dealloy behaviours of the newly formed Sn with Li leads to the birth and extinction of $Li_{4.4}Sn$, and the Li_2S acts as an inert matrix surrounding the active Sn nanograins.[16] By this mechanism, Sn endows SnS_2 with a theoretical capacity of 645 mA h g^{-1}, which is rather smaller than that of pure Sn (993 mA h g^{-1}) and SnO_2 (781 mA h g^{-1}).

Fig. 9c displays capacities of the two SnS_2 electrodes over 50 electrochemical cycles at 100 mA g^{-1} in a potential range from 0.01 to 1.2 V *versus* Li/Li^+. The charge capacity of SnS_2 anode rises somewhat in the first five cycles, but that of SnS_2/CNTs electrode does not, indicating that a Li-ion insertion activation process is negligible in the latter due to fast Li-ion transfer in a 2D nanostructure. In general, the SnS_2/CNTs electrode delivers significantly better cyclability than the bare SnS_2 electrode. As shown in the figure, the former shows a final charge capacity of 373.1 mA h g^{-1} that is 91.5% of its initial charge capacity. On the contrary, the latter exhibits a final capacity of 200.7 mA h g^{-1} which is only 66.8% of its initial charge capacity. The poorer cycling performance of pure SnS_2 anode is attributed to its intrinsically low electronic conductivity and internal damage from large volume expansion in the alloying of Li into metallic Sn. This result proves that the strategy of composite with CNTs is as effective as carbon coatings[15] or coatings on CNTs[17,18] to strengthen the stability of SnS_2 anodes in durable LIBs. It is worth noting that the two anodes have close capacities in the early cycling stage, which might be ascribed to the addition of superfluous MWCNTs with low capacity (<200 mA h g^{-1})[17] into SnS_2. As a result, work is in progress to optimize CNTs content in the SnS_2/CNTs composite, aiming for both larger capacities and better cyclability of SnS_2 anodes.

We also studied the rate performance of SnS_2 and SnS_2/CNTs anodes. It can be seen from Fig. 9d and e that the electrode polarization is increased faster for the SnS_2 anode than for the SnS_2/CNTs anode as the current goes up for tests, suggesting better conductivity of the SnS_2/CNTs electrode. Consequently, the capacity of the latter becomes higher than that of pure SnS_2 at various current densities from 100 to 1000 mA g^{-1} (Fig. 9f). In particular, the capacity of SnS_2/CNTs anode is five times of that of SnS_2 anode at a large current of 1000 mA g^{-1}.

The Li-ion intercalation behaviors at the two anodes are again examined by their differential capacity curves (Fig. 10a and b) derived from their discharge–charge plots. Clearly, both

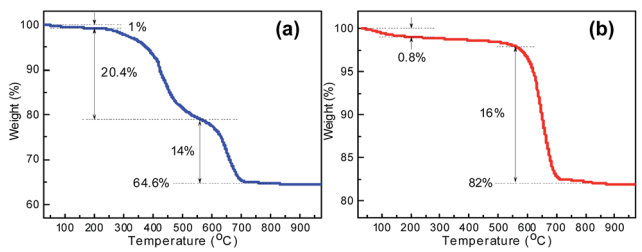

Fig. 7 TGA of (a) SnS_2/CNTs and (b) SnO_2/CNTs hybrids.

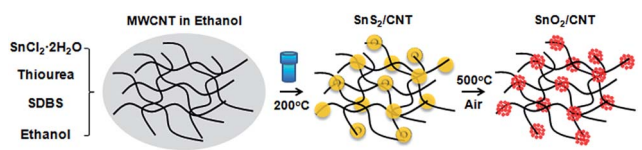

Fig. 8 Schematic illustrating the growth of SnS_2/CNTs and SnO_2/CNTs composites.

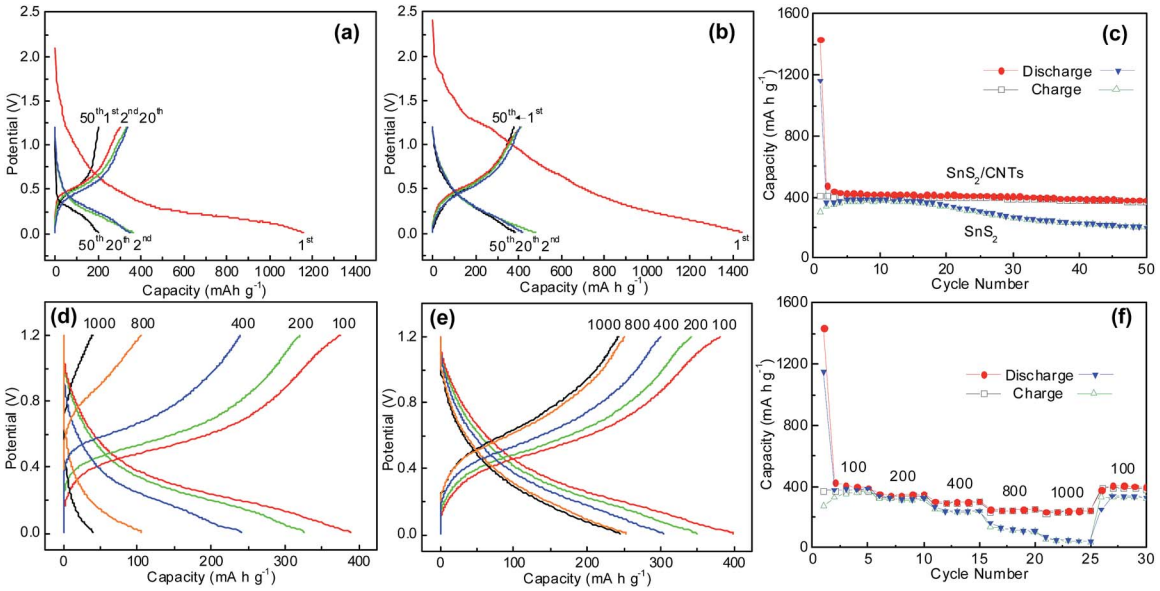

Fig. 9 Charge–discharge plots of (a) SnS_2 and (b) SnS_2/CNTs composite and (c) their cycling at 100 mA g^{-1}; charge–discharge plots of (d) SnS_2 and (e) SnS_2/CNTs composite when cycled at different current densities and (f) their rate capability.

of them have one broad reduction peak in the cathodic scan and one broad oxidation peak in the anodic scan. The position of the peaks is almost the same (0.05–0.39 V, 0.4–0.7 V), but the reduction peak of the SnS_2/CNTs anode starts about 0.6 V and gradually rises, while that of SnS_2 anode sharply increases at a lower potential of about 0.45 V, suggesting smaller polarization and better reversibility of Li-ion insertion/extraction reaction at the SnS_2/CNTs anode. In addition, the estimated integral area (representing their specific capacity) between the discharge and charge plots in the whole potential range is clearly larger for the composite electrode than for the SnS_2, suggesting that more electrons and Li^+ ions involve the insertion/extraction process in the former. In order to verify these points, EIS technique is employed to explore Li-ion transfer kinetics at the SnS_2 and SnS_2/CNTs anodes. Fig. 10c shows Nyquist plots and their equivalent circuit after the cells were discharged and charged for ten cycles. A small depressed semicircle is found at high frequency region in both curves, indicating the formation of a passivating SEI film on the anode surface. A second depressed semicircle is seen in the high-to-medium frequency region, which denotes the charge transfer progress between the active material and electrolyte. In the low frequency region, the straight line displays characteristics of Warburg impedance (W) that generally reflect the Li-ion diffusion behaviours within particles of the active material. In the circuit, R_Ω is the ohmic resistance derived from the organic electrolyte, separator and electrodes, corresponding to the intercept of the first depressed semicircle with Z-real axis. As for the first semicircle, R_s represents the resistance of Li-ion diffusion through the SEI layer; CPE_s is the constant phase-angle element depicting the non-ideal capacitance resistance. For the second semicircle, R_{ct} is the charge transfer resistance, and CPE_{dl} is the constant phase-angle element that is related to a double layer capacitance. It is easily found that R_{ct} is significantly larger for the bare SnS_2 anode than for the SnS_2/CNTs electrodes, which reflects rapider charge transfer or lower charge transfer resistance in the latter.

In addition to the optimization of MWCNTs content in the SnS_2/CNTs composite, the oxidation of SnS_2 to SnO_2 could be an alternative route to improve the specific capacity of the anode, due to their theoretical capacity difference. Hence, we for the

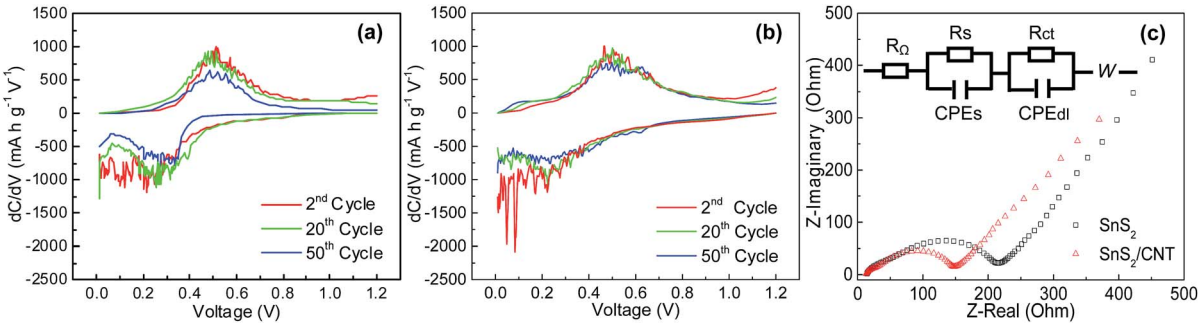

Fig. 10 Differential capacity plots of (a) SnS_2, (b) SnS_2/CNTs composite, and (c) Nyquist plots and equivalent circuit.

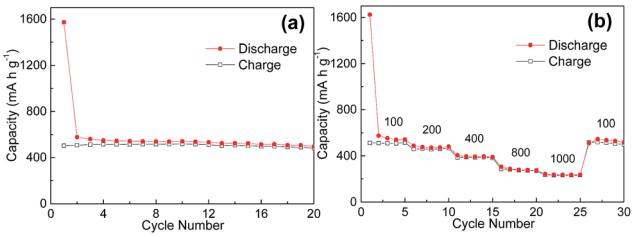

Fig. 11 (a) Cyclability and (b) rate capability of SnO_2/CNTs composite electrode.

first time achieved a porous thin SnO_2 nanoflake/CNTs hybrid readily by annealing the as-obtained SnS_2/CNTs. Fig. 11a shows the good cycling performance of SnO_2/CNTs anode at 100 mA g^{-1} over 20 cycles. Apparently, its capacity of about 500 mA h g^{-1} exceeds that of SnS_2/CNTs anode by almost 100 mA h g^{-1}, let alone graphite with an even lower capacity. The SnO_2/CNTs electrode also delivers excellent rate capability at various current from 100 to 1000 mA g^{-1} (Fig. 11b). The results demonstrate that a hybrid structure made of 2D active material (*e.g.* metal oxides and sulfides) and conductive carbon network is an ideal candidate for high-performance LIB electrodes.

3. Conclusions

SnS_2 nanoparticles and SnS_2 nanoflake/CNTs composite were prepared by a simple hydrothermal approach. The addition of conducting MWCNTs for the synthesis was found to affect the morphology of obtained SnS_2 nanostructures. Dispersed CNTs in solutions restrain their growth and yield the formation of 2D SnS_2 nanoflakes enwrapped by MWCNTs, rather than irregular SnS_2 nanoparticles, eventually to achieve a 3D porous structure with larger surface area. Firstly, those nanoflakes shorten paths for Li-ion transfer and thus reduce the ionic transfer resistance. Secondly, the embedment of SnS_2 nanoflakes into a conductive MWCNT matrix allows fast electronic diffusion and effectively cushions the volume change of SnS_2 during cycling. All these unique properties lead to the significantly better cyclability and rate performance of SnS_2/CNTs composite than that of the SnS_2 nanoparticle anode. The composite can be fully changed to 2D SnO_2 nanoflake/CNTs hybrid *via* annealing in air, which shows increased Li-ion storage capacities. Our results demonstrate that metal oxides and sulphides that are integrated with conducing MWCNTs and therefore harvest enhanced Li-ion intercalation properties could be a promising material for the anode of high-performance LIBs.

4. Experimental details

MWCNTs (outer diameter of 6–9 nm, length of 5 μm, Sigma Aldrich) were first added into nitric acid and stirred overnight, then filtered and washed with de-ionized water and absolute ethanol (≥99.5%, Sigma Aldrich), and dried in a vacuum oven. 0.009 g CNTs and 1 g sodium dodecylbenzenesulfonate (SDBS) powder were put into a glass beaker containing 60 ml anhydrous ethanol, ultrasonically treated until a homogenous black solution was obtained. Later, 0.001 mol $SnCl_2 \cdot 2H_2O$ and 0.004 mol thiourea powder were added into the CNTs solution. After vigorously stirring for 15 min, the solution was transferred into a Teflon-lined autoclave of 100 ml capacity, and then the autoclave was sealed and heated at 200 °C for 24 h. A black precipitate was yielded and collected by centrifugation, rinsed with distilled water and ethanol for six times. The final product was dried at 80 °C in the vacuum oven overnight. For comparison, SnS_2 particles were produced in the same route but without the addition of CNTs. The obtained SnS_2/CNTs product was further annealed at 500 °C in air for 1 h to gain SnO_2/CNTs composites.

A Hitachi S-4800 scanning electron microscope (SEM) and a Hitachi H9000NAR transmission electron microscope (TEM) were used to observe these materials. Their crystallographic structure was determined by X-ray diffraction (XRD) using a Scintag XDS 2000 X-ray diffractometer with Cu K_α radiation at a scan rate of 2° min^{-1}. Chemical composition of these particles was characterized by an energy dispersive X-ray spectroscopy (EDS) with an XFlash detector (Bruker AXS), and an X-ray photoelectron spectroscope (XPS, Perkin-Elmer PHI 5400 ESCA System) using a monochromatized Mg K_α X-ray radiation source. Thermogravimetry analysis (TGA) was carried out on a simultaneous thermal analyzer (TA Instruments, SDT 2960) in an air atmosphere from room temperature to 1000 °C at a rate of 20 °C min^{-1}. The Brunauer–Emmett–Teller (BET) surface area were measured by a surface area and porosity analyzer (MICROMERITICS, ASAP 2020).

Cu foils (12 μm thick) were cleaned with acetone and dried in air. A slurry was made from a mixture of the prepared material, carbon black (99.5%, Alfa Aesar), and polyvinylidene fluoride (4 wt% in *N*-methyl-2-pyrrolidone) in a weight ratio of 80 : 10 : 10. The slurry was then spread on the copper foil using a blade casting method, followed by drying in air at room temperature and in vacuum at 100 °C for 12 h. Later, the Cu foil was cut into disks with a diameter of 3/8 inch that were then pressed by a Carver Lab Press with a pressure of 6 MPa. Masses of the active material are about 1 mg. CR2032 coin cells were assembled to investigate battery behaviours of the samples acting as the working electrode. A lithium disc is used as the counter and reference electrode in the cells, which was separated from the working electrode by a Celgard-2320 separator. The organic electrolyte was 1 mol L^{-1} $LiPF_6$ dissolved in a mixed solvent of ethylene carbonate and diethylene carbonate with 1 : 1 volume ratio (Novolyte Technologies, Inc.). All the coin cells were assembled in an Ar-filled glove box with oxygen and moisture levels lower than 1 ppm. The galvanostatic charge–discharge was carried out on LANHE automatic battery testers at 100 mA g^{-1} current for 50 cycles or 100–1000 mA g^{-1} for 30 cycles. AC impedance measurements were also conducted on these cells at a potential of ~0.4 V from 100 kHz to 0.01 Hz with a perturbation of 5 mV applied.

Acknowledgements

Financial supports from the University of Wisconsin System Applied Research program and the University of Wisconsin–

Milwaukee Bradley and Hertz Catalyst Grant Programs are gratefully acknowledged.

Notes and references

1 J. M. Tarascon and M. Armand, *Nature*, 2001, **414**, 359.
2 A. S. Arico, P. Bruce, B. Scrosati, J. M. Tarascon and W. Van Schalkwijk, *Nat. Mater.*, 2005, **4**, 366.
3 J. Li, Y. Hou, X. Gao, D. Guan, Y. Xie, J. Chen and C. Yuan, *Nano Energy*, 2015, **16**, 10.
4 Q. Wang, Q. Wang, D. A. Zhang, J. Sun, L. L. Xin and X. Y. Xue, *Chem.–Asian J.*, 2014, **9**, 3299.
5 Q. Wang, D. A. Zhang, Q. Wang, J. Sun, L. L. Xin and X. Y. Xue, *Electrochim. Acta*, 2014, **146**, 411.
6 Q. Wang, J. Sun, Q. Wang, D. A. Zhang, L. L. Xin and X. Y. Xue, *J. Mater. Chem. A*, 2015, **3**, 5083.
7 M. K. Jana, H. B. Rajendra, A. J. Bhattacharyya and K. Biswas, *CrystEngComm*, 2014, **16**, 3994.
8 S. H. Chaki, M. P. Deshpande, D. P. Trivedi, J. P. Tailor, M. D. Chaudhary and K. Mahato, *Appl. Nanosci.*, 2013, **3**, 189.
9 J. Seo, J. Jang, S. Park, C. Kim, B. Park and J. Cheon, *Adv. Mater.*, 2008, **20**, 4269.
10 T. J. Kim, C. Kim, D. Son, M. Choi and B. Park, *J. Power Sources*, 2007, **167**, 529.
11 D. Ma, W. Zhang, Q. Tang, R. Zhang, W. Yu and Y. Qian, *J. Nanosci. Nanotechnol.*, 2005, **5**, 806.
12 S. Liu, X. Yin, L. Chen, Q. Li and T. Wang, *Solid State Sci.*, 2010, **12**, 712.
13 P. Wu, N. Du, H. Zhang, J. Liu, L. Chang, L. Wang, D. Yang and J. Z. Jiang, *Nanoscale*, 2012, **4**, 4002.
14 K. Chang, Z. Wang, G. Huang, H. Li, W. Chen and J. Y. Lee, *J. Power Sources*, 2012, **201**, 259.
15 H. S. Kim, Y. H. Chung, S. H. Kang and Y. E. Sung, *Electrochim. Acta*, 2009, **54**, 3606.
16 M. He, L. X. Yuan and Y. H. Huang, *RSC Adv.*, 2013, **3**, 3374.
17 C. Zhai, N. Du, H. Zhang, J. Yu and D. Yang, *ACS Appl. Mater. Interfaces*, 2011, **3**, 4067.
18 H. Sun, M. Ahmad, J. Luo, Y. Shi, W. Shen and J. Zhu, *Mater. Res. Bull.*, 2014, **49**, 319.
19 J. G. Kang, G. H. Lee, K. S. Park, S. O. Kim, S. Lee, D. W. Kim and J. G. Park, *J. Mater. Chem.*, 2012, **22**, 9330.
20 D. A. Zhang, Q. Wang, Q. Wang, J. Sun, L. L. Xing and X. Y. Xue, *Mater. Lett.*, 2014, **128**, 295.
21 M. O. Guler, O. Cevher, T. Cetinkaya, U. Tocoglu and H. Akbulut, *Int. J. Energy Res.*, 2014, **38**, 487.
22 D. Su, H.-J. Ahnb and G. Wang, *Chem. Commun.*, 2013, **49**, 3131.
23 L. Zhu, W. Wu, Y. Zhu, W. Tang and Y. Wu, *J. Phys. Chem. C*, 2015, **119**, 7069.
24 X. Zhou, Z. Xia, Z. Zhang, Y. Ma and Y. Qu, *J. Mater. Chem. A*, 2014, **2**, 11799.
25 J. Huang, K. Yu, C. Gu, M. Zhai, Y. Wu, M. Yang and J. Liu, *Sens. Actuators, B*, 2010, **147**, 467.
26 Y. Z. Zhang, H. Pang, Y. Sun, W. Y. Lai, A. Wei and W. Huang, *Int. J. Electrochem. Sci.*, 2013, **8**, 3371.
27 J. Liu, J. Liu, W. Song, F. Wang and Y. Song, *J. Mater. Chem.*, 2014, **2**, 17477.
28 A. M. Baker, L. Wang, S. G. Advani and A. K. Prasad, *J. Mater. Chem.*, 2012, **22**, 14008.
29 H. Zhong, G. Yang, H. Song, Q. Liao, H. Cui, P. Shen and C. X. Wang, *J. Phys. Chem. C*, 2012, **116**, 9319.
30 D. Guan, J. Li, X. Gao and C. Yuan, *J. Alloys Compd.*, 2014, **617**, 464.